Supplemental Information: Fe-Substituted Sodium β"-Al$_2$O$_3$ as a High-Rate Na-ion Electrode

Danielle Butts[1], Jürgen Schoiber[2], Christopher Choi[1], Günther J. Redhammer[2], Nicola Hüsing[2]

Scott Donne[3], Bruce Dunn[1*]

[1] Department of Materials Science and Engineering, University of California, Los Angeles, California 90095, USA

[2] Chemistry and Physics of Materials, University of Salzburg, 5020 Salzburg, Austria

[3] Discipline of Chemistry, University of Newcastle, Callaghan NSW 2308, Australia
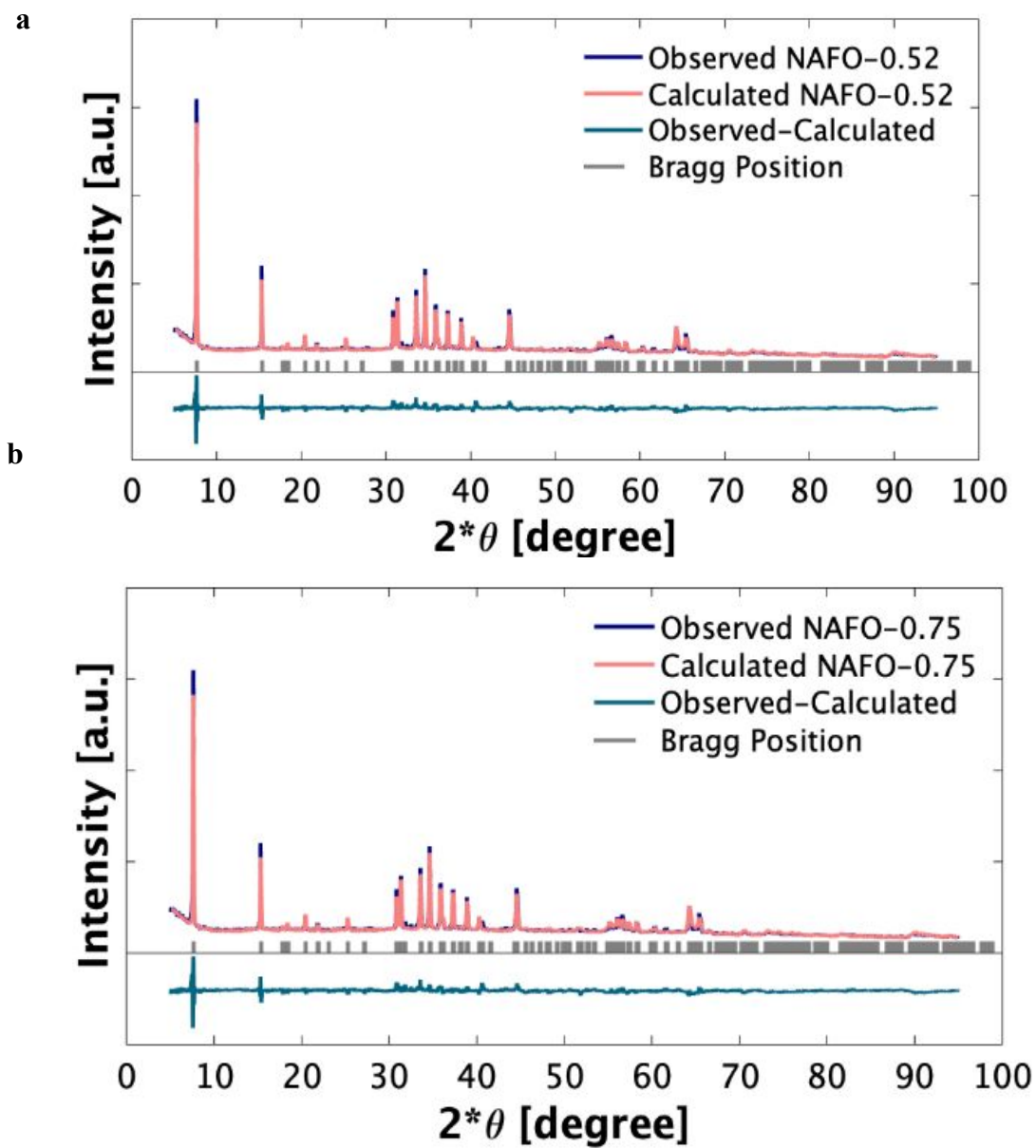
*Corresponding author email: bdunn@ucla.edu

Figure S1. Rietveld refinements of **a)** NAFO-0.52 and **b)** NAFO-0.75 powder diffractograms shown here are used to calculate the Fe site occupancy.
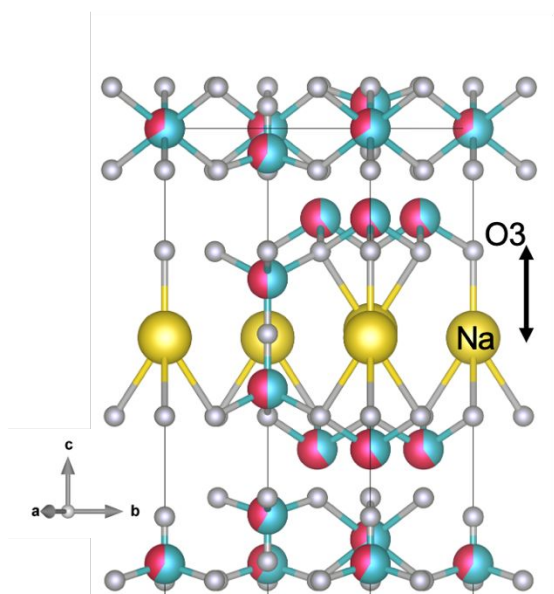
Figure S2: a*-axis view of NAFO-0.52, showing the O3-Na bond used to calculate the conduction plane thickness. The calculated bond distances are outlined in Table S1. [Na (yellow), O (gray) Al (blue) Fe (red)]

Table S1. Bond lengths from O3 on the edge of the spinel block to Na in the center of the conduction plane (Figure S2) for NAFO-0.52, NAFO-0.75, and undoped $Na_{1.77}Al_{11}O_{17}$ for reference.

Composition	O3 to Na1 bond length [Å]
$Na_{1.77}Al_{11}O_{17}$ [a]	2.54
NAFO-0.52	2.44
NAFO-0.75	2.14

[a] From single crystal measurements [1]

Table S2. Inductively coupled plasma mass spectrometry (ICP-MS) measurements on NAFO-0.52 and NAFO-0.75 highlighting the similar Fe:Al molar ratios to those calculated through Rietveld refinement (Table 1).

Sample	Iron [wt. %]		Aluminum [wt. %]		Average Fe_xAl_y molar ratio	
	Average*	stdev	Average*	stdev	x	y
NAFO-0.52	31.32	1.44	15.91	0.87	0.49	0.51
NAFO-0.75	47.92	1.03	6.55	0.27	0.78	0.22

Each sample was done in triplicated measurements with background correction.
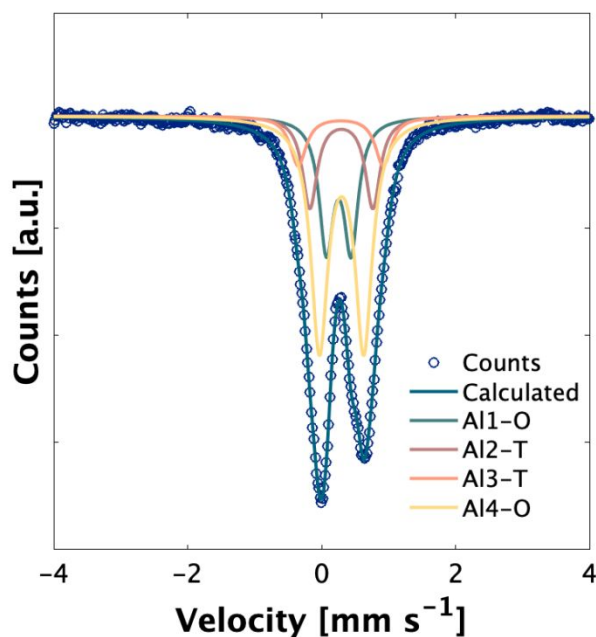
3

Figure S3. [57]Fe Mössbauer spectrum of NAFO-0.52, recorded at 298 K and evaluated with 4 Lorentzian shaped doublets. The Fe occupancy obtained from Mössbauer fitting closely matches Fe occupancy obtained through Rietveld refinement and suggests that Fe is in the 3+ valence state after synthesis.

Table S3. Fe site occupancy of NAFO-0.52 as determined by Mössbauer spectroscopy.

Site (coordination)[a]	Isomer Shift [mm s^{-1}]	Quadrupole Splitting [mm s^{-1}]	Amount [%]
1 (O)	0.299	0.661	50
2 (T)	0.286	1.270	10
3 (T)	0.295	0.941	17
4 (O)	0.256	0.369	23

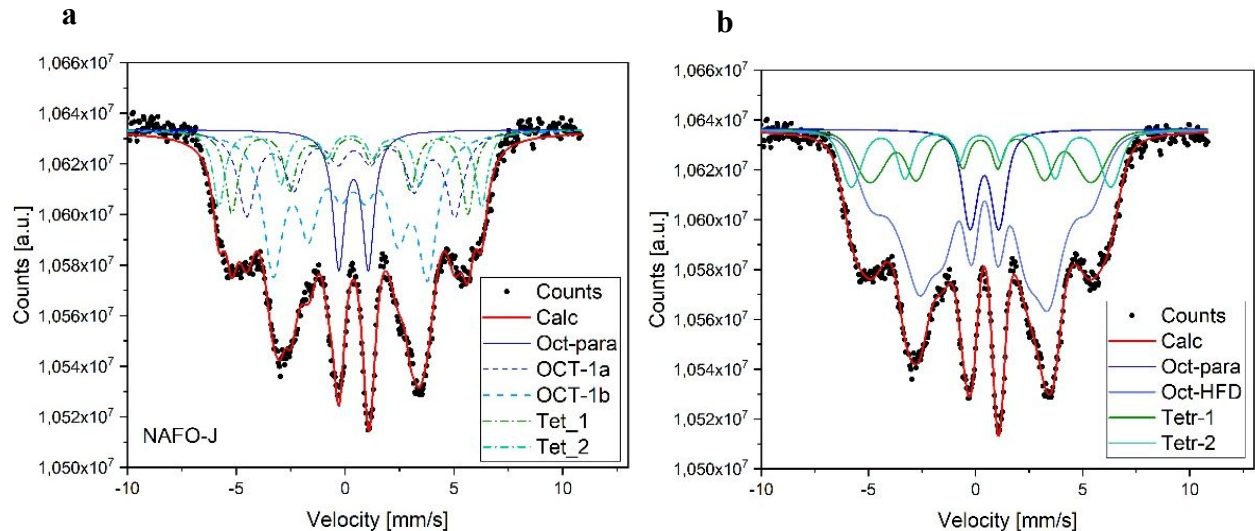[a] Coordination is either octahedral (O) or tetrahedral (T) for Fe sites.

Figure S4: a) [57]Fe Mössbauer spectrum of NAFO-0.75 powder, recorded at 298 K and evaluated with an exact line shape full static Hamiltonian approach and b) and a hyperfine field distribution approach. The fittings utilized 5 components: one paramagnetic doublet octahedral site (Oct-para), two identical octahedral sties with hyperfine field distributions (Oct-HFD), and two tetrahedral sites (Tet-1 and Tet-2). Due to the low resolution of the spectra and the complicated nature of magnetic interactions within the structure, site occupancy calculations were not possible.

Mössbauer Spectroscopy

[57]Fe Mossbauer spectroscopy was performed in an attempt to determine the valence state of Fe in the NAFO-0.52 and -0.75 as-synthesized materials. The main component of the NAFO-0.52 Mössbauer spectrum (Figure S3) corresponds to Fe^{3+} in a regular octahedral coordination, site 1(O) in Table S3, based on the quadrupole splitting value of ~ 0.6 mm s^{-1}. The second octahedral component, site 4(O) in Table S3, with a distinctly lower occupancy has a somewhat more distorted local distortion environment. On the two tetrahedral sites, site 2 and 3 in Table S3, both have lower Fe^{3+} occupancy than the octahedral sites with a larger locally distorted environment for site 2(T) than site 3(T). Thus, a fairly good agreement between iron site population by Mössbauer spectroscopy (Table S3) and Rietveld refinement (Table 1) is obtained despite the errors associated with the large overlap of individual components in the Mössbauer spectrum.

The higher Fe content NAFO-0.75 displays a much more complicated ^{57}Fe Mössbauer spectrum due to the observed magnetic hyperfine interactions at room temperature. **Figure S4** displays the two attempted fittings of the NAFO-0.75 Mössbauer spectrum based on a classical Hamiltonian approach with Lorentzian shaped lines and a hyperfine field distribution approach. Adequate refinements were achieved using four magnetic split sextets for Fe^{3+} (two ascribed to the octahedral and two to the tetrahedral sites based on the Mössbauer parameters). Additionally, one paramagnetic doublet, which is low in relative area fraction, is ascribed to Fe^{3+} in octahedral coordination. There is no firm evidence for the presence of Fe^{2+}. As only four sites are available in the structure, but a minimum of 5 components are needed for adequate refinement, it was assumed that two of the magnetic split components both belong to Fe^{3+} in the same octahedral site. The paramagnetic doublet site is ascribed to the other octahedral site which shows mainly an occupation with Al^{3+}. Due to the low Fe content at this site, the magnetic super-exchange is most likely hindered. For the two remaining magnetic components, the refined isomer shift clearly indicates tetrahedral coordination although the quadrupole splitting is high. This may suggest that there is a distorted Fe tetrahedral site, but also may be due to an artefact because of the high correlation between the internal magnetic field $H_{f,eq}$. Based on the low resolution and magnetic hyperfine distribution effects, observed in the broad resonance absorption lines, more detailed refinement and site occupancy calculations were not possible.

Diffusion Coefficient Calculation

The diffusion coefficient was calculated from the ionic conductivity to compare the diffusion coefficient of NAFO-0.52 to other high-rate electrode materials. The Nernst-Einstein relation can be used to calculate a Na^+ diffusion coefficient through the bulk of the material as[2]

$$D_{Na^+} = \frac{\sigma_{b,Na^+} RT}{C_{Na^+} F^2} \qquad \text{Eq. S1}$$

where R is the gas constant, T is temperature, c_{Na^+} is the molar concentration of Na^+ per unit volume obtained from Rietveld refinement, and F is Faraday's constant. The diffusion coefficient of Na^+ in NAFO-0.52 is calculated to be 9 x 10^{-8} cm^2 s^{-1}, well surpassing the diffusion coefficient of ~10^{-10} cm^2 s^{-1} typically observed in NASICON type materials[3] (for $Na_3V_2(PO_4)_3$, $D_{Na^+} \approx 10^{-10}$ cm^2 s^{-1} [REF 4] and for $NaTi_2(PO_4)_3$, $D_{Na^+} \approx 10^{-12}$- 10^{-13} cm^2 s^{-1} [REF 5]).

Table S4. Conductivities and diffusion coefficients of materials discussed throughout the text.

| Material	Conductivity [S cm^{-1}]		Diffusion Coefficient [cm^2 s^{-1}]	Test environment, technique	Electrolyte, Electrode	REF
	Ionic	Electronic				
$Na_3V_2(PO_4)_3$@C/G	---	---	4.59 x 10^{-10}	25 °C; 1 M NaClO$_4$ in EC/DEC (1:2; v/v) with 2 vol.% FEC, EIS	Electrode	[4]
P2-$Na_{2/3}Ni_{1/3}Mn_{1/3}Ti_{1/3}O_2$	---	---	10^{-10} - 10^{-9}	RT, 1M NaClO$_4$ in EC/DEC (1:1; v/v) with 5 vol.% FEC, GITT	Electrode	[6]
$Na_3V_2(PO_4)_3$	~10$^{-6.5}$	---	6×10^{-13} – 2×10^{-15} cm^2 s^{-1}	- Polycrystalline, RT, EIS - RT, 1 M NaPF$_6$ in propylene carbonate (PC), GITT	Electrode	[7,8]
$Na_3Fe_2(PO_4)_3$	---	---	2.4 × 10^{-8} cm^2 s^{-1}	RT, 1M NaClO$_4$ in EC/DMC (1:1; v/v), CV	Electrode	[9]
$Na_3Fe_2(PO_4)P_2O_7$@RGO	---	---	1 × 10^{-11} – 5 × 10^{-10} cm^2 s^{-1}	RT, 1M NaClO$_4$ in EC/DEC (1:1; v/v) 5% FEC, GITT	Electrode	[10]
$NaTi_2(PO_4)_3$	---	---	~4 × 10^{-15} cm^2 s^{-1}	RT, 1M NaClO$_4$ in EC/DMC (1:1; v/v), CV	Electrode	[11]
T-Nb_2O_5	---	3 x 10^{-5}	---	Polycrystalline 300K, four-point probe	Electrode	[12]
TiO_2(B)	---	8 x 10^{-5}	---	Polycrystalline, Room Temperature	Electrode	[13]
$Na_{1+x}Ti_{2-x}Al_x(PO_4)_3$ x = 0.6 – 0.9	1.3 x 10^{-7}	---	---	Polycrystalline, RT	Electrolyte	[14]
$Na_{1+x}Zr_2P_{3-x}Si_xO_{12}$ $0 \leq x \leq 3$	6.7 × 10^{-4}	---	---	Polycrystalline, Room Temperature, EIS	Electrolyte	[15]
$Na_{3.1}Zr_{1.95}Mg_{0.05}Si_2PO_{12}$	~3.5 × 10^{-3}	---	~5 × 10^{-8}	Polycrystalline, Room Temperature, EIS, CV	Electrolyte	[16]
Li_3N	6.6 x 10^{-4}	---	---	Polycrystalline at 25 °C, EIS	Electrolyte	[17]
$Na_{1.67}Li_{0.33}Al_{11}O_{17}$	1 x 10^{-3}	---	---	Polycrystalline β" at 25 °C	Electrolyte	[18]
NAFO-0.52	1.7 x 10^{-3}	1.2 x 10^{-7}	9 x 10^{-8}	Polycrystalline 25 °C, EIS	Electrode	This work
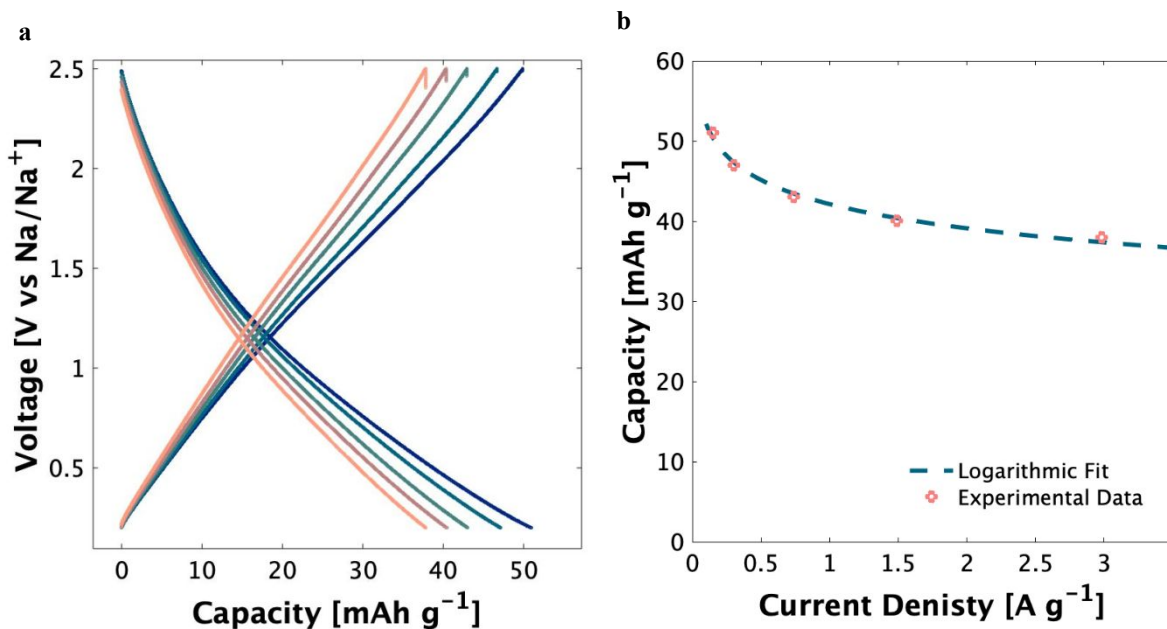
Figure S5. a) Galvanostatic cycling of Ketjen black:PVDF 80:20 electrode with ~0.5 mg cm^{-2} loading on Cu at a current of 0.15, 0.30, 0.74, 0.49, and 2.98 A g^{-1}. The capacity obtained from Ketjen black at each applied current density is used to obtain a logarithmic fit. (b) The logarithmic equation is then used to calculate the capacity from carbon at the current density applied to the composite electrode. The capacity from carbon is then subtracted from the composite electrode to obtain only the capacity from the active material (Figure 4).

Table S5. Na and Fe atom % determined by energy dispersive X-ray analysis on ex-situ NAFO-0.52 electrodes (pristine, cycled to 2.5 V, and cycled to 0.2 V). Electrodes were soaked in DMC and dried in an Ar atmosphere prior to measurements. Average atom % is used to calculate an average Na:Fe ratio for each electrode. The difference between the Na:Fe ratio in the electrode cycled to 2.5 V and 0.2 V is used to calculate the mol Na inserted per formula unit into NAFO-0.52 with 5.72 mol Fe per formula unit. The amount of Na in the pristine electrode is calculated for comparison.

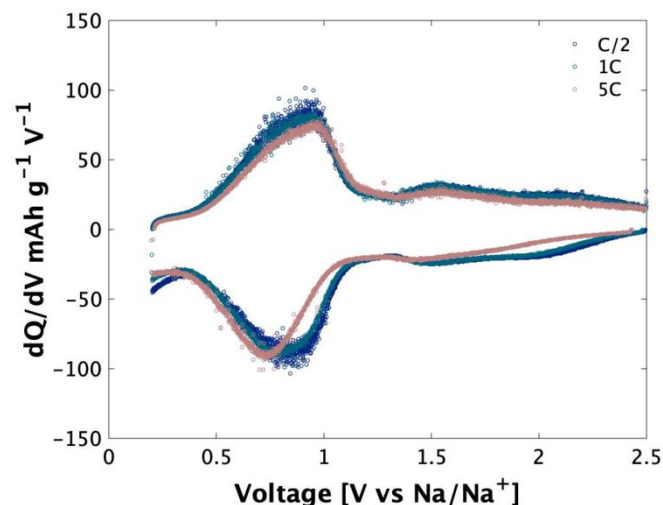| EDX Map #	Element	Pristine	Cycled to 2.5 V	Cycled to 0.2 V
		Atom %		
Map 1	Fe	5.15	1.77	4.71
	Na	1.83	5.92	12.03
Map 2	Fe	5.01	1.31	3.59
	Na	1.86	3.91	11.25
Map 3	Fe	3.86	1.64	3.49
	Na	1.66	4.85	12.11
Map 4	Fe	4.81	2.64	--
	Na	1.72	7.96	--
Map 5	Fe	--	3.29	--
	Na	--	9.51	--
Map 6	Fe	--	3.29	--
	Na	--	10.2	--
Map 7	Fe	--	4..93	--
	Na	--	8.70	--
Average Na:Fe		0.37	2.71	3.00
Calculated mol Na inserted based on 5.72 Fe per formula unit		2.13	1.67	

9

Figure S6. Change in charge stored with voltage during galvanostatic cycling, dQ/dV, for NAFO-0.52 at charge rates of C/2, 1C, and 5C, displaying the broad redox peak between 0.3 and 1.2 V vs Na/Na$^+$ similar to that observed in cyclic voltammetry (Figure 5a).
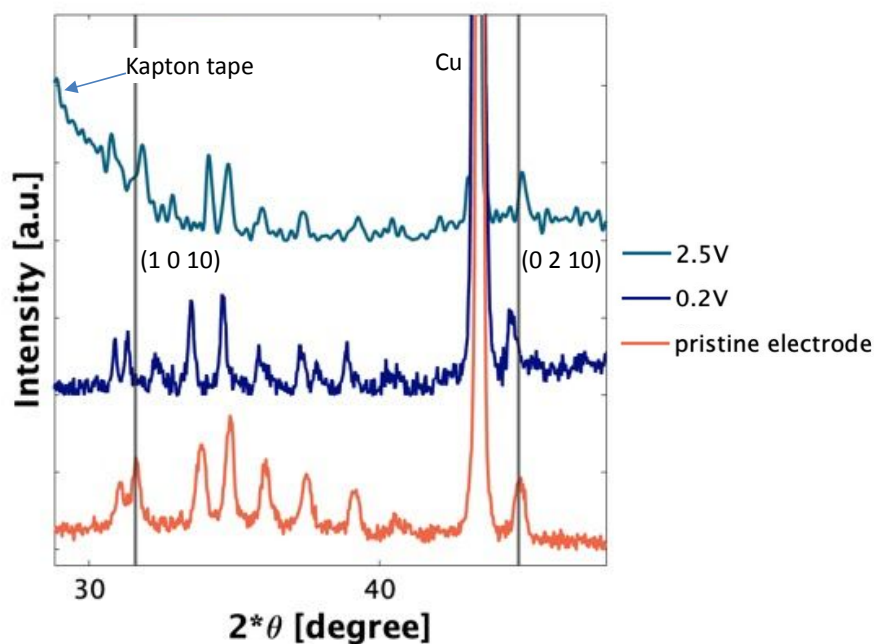

Figure S7. Comparison of the X-ray diffraction pattern of a pristine, uncycled electrode and electrodes galvanostatically cycled to 0.2 V (1st cycle) and 2.5 V vs Na/Na$^+$ (10th cycle). The shifts in peak positions indicate a compression of the unit cell upon Na removal to 2.5 V and expansion of the unit cell upon Na insertion to 0.2 V, highlighted by the vertical lines at the (1 0 10) and (0 2 10) reflections and corresponding shifts of the 0.2 and 2.5 V reflections. The 0.2 V diffraction pattern demonstrates that there is no obvious structural breakdown or conversion reaction that occurs at low voltages such as the formation of Fe$_2$O$_3$ or

Na-metal. The small peak at ~32° 2θ reveals that a small amount of the β'' phase has been converted to the β phase, which does not appear to significantly affect cycling behavior due to the capacity retention and high Coulombic efficiency (Figure S9).

Table S6. Lattice parameters of NAFO-0.52 before cycling and after 10 cycles at 1C, highlighting the structural stability after sodium insertion and de-insertion.

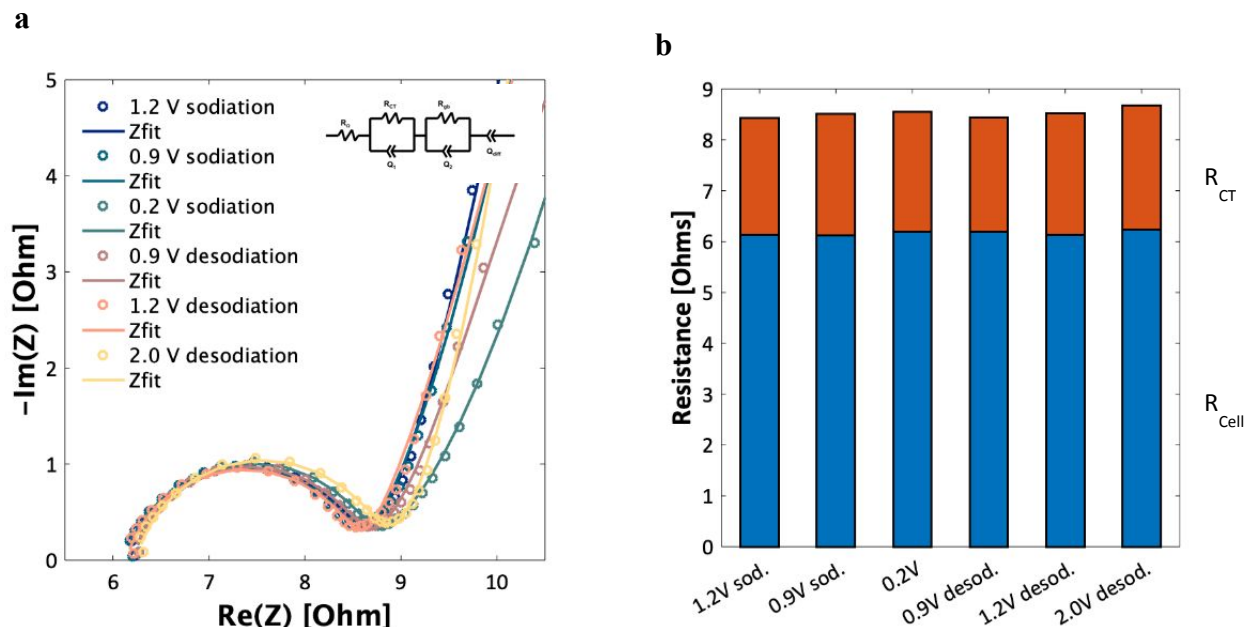| Lattice Parameter	Pristine	10 cycles at 1C
a [Å]	5.79	5.79
c [Å]	34.66	34.75
V [Å³]	1007.32	1007.51

a

b

Figure S8. a) Electrochemical impedance spectroscopy (EIS) of an NAFO-0.52 vs Na metal coin-cell with corresponding equivalent circuit fitting (shown in the inset). EIS spectra were obtained after holding for 30 min at the indicated voltage to reach an equilibrium state. Throughout cycling, the cell resistance R_{cell} and charge transfer resistance R_{CT} remain stable (b), suggesting the absence of interfacial reactions or secondary phase formation.
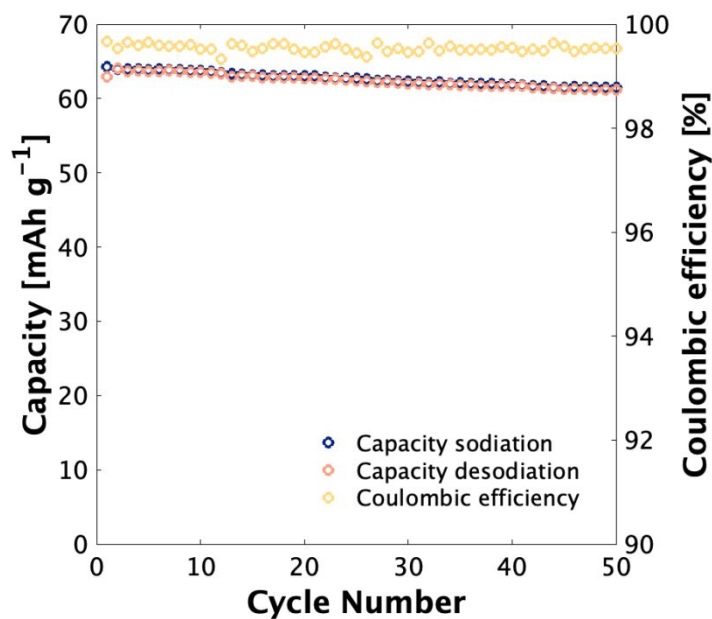
Figure S9. NAFO-0.52 galvanostatic cycling sodiation (blue) and desodiation (pink) capacity at a 1C-rate (after galvanostatic rate cycling shown in Figure 5a) with corresponding Coulombic efficiency (yellow), indicating > 95 % capacity retention over 50 cycles and > 99 % efficiency.
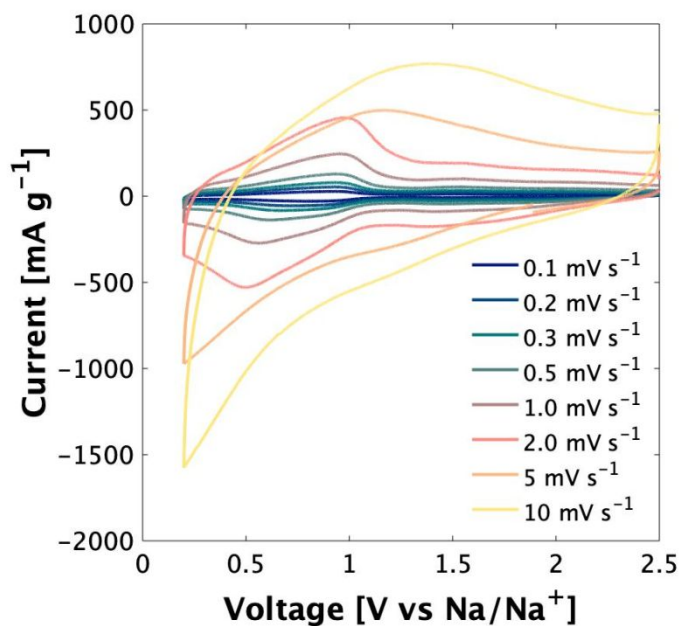

Figure S10. Cyclic voltammetry of NAFO-0.52 from 0.1mV s^{-1} to 10 mV s^{-1}.

Step Potential Electrochemical Spectroscopy

In order to gain more quantitative insight into the nature of the capacitive vs diffusion controlled currents, step potential electrochemical spectroscopy (SPECS) can be used to model the capacitive and diffusion-controlled currents at each potential.[19,20] In this method, a 10 mV potential step is applied and the current response is measured while holding at that potential for an equilibration period of 300 seconds. This is repeated throughout the entire potential window such that each potential step can be taken as a jump in voltage from an equilibrium current value. The current response can then be modeled using two capacitive current models, a diffusion-limited current model, and a residual current based on the small but non-zero current value after 300 seconds. The two modeled capacitive currents represent the geometric capacitive current i_g [A g⁻¹] (from the electrode-electrolyte surface) and the porous capacitive current i_p [A g⁻¹] (from the internal interfaces of the electrode):

$$i_g = \frac{\Delta E}{R_1}\exp\left(-\frac{t}{R_1 C_1}\right),$$

Eq. S2a

$$i_p = \frac{\Delta E}{R_2}\exp\left(-\frac{t}{R_2 C_2}\right),$$

Eq. S2b

where ΔE is the voltage step size [V], R is resistance [$\Omega \cdot$ g], C is capacitance [F g⁻¹], and t is time [s]. The diffusion-controlled current can be modeled from the Cottrell equation for semi-infinite planar diffusion[21]:

$$i_d = \frac{B}{t^{1/2}} \text{ [A g}^{-1}]$$

Eq. S3

where B is a fitting parameter. The total current at each voltage step can then be taken as

$$i_{Total} = i_g + i_p + i_d + i_r,$$

Eq. S4

where i_r [A g⁻¹] is the residual current. Given this model of a time-dependent current response throughout the voltage window, the current response can then be reevaluated at an assumed sweep rate to give a calculated cyclic voltammogram.[22] The reconstructed CV of NAFO-0.52 at 0.01 mV s⁻¹ is shown in **Figure S11a**, demonstrating the high values of i_p (the capacitive current within the electrode) throughout the redox process from 0.5 to 1.2 V vs Na/Na⁺. Comparing the calculated SPECS voltammogram at 0.001 mV s⁻¹ and the experimental data collected at a sweep rate of 0.1

mV s^{-1}, the SPECS analysis does an excellent job of capturing the electrochemical features of the Fe^{3+}/Fe^{2+} redox. An example of a modeled current response is shown in **Figure S11b and c**.

Now, with experimental CV measurements at sweep rates from 0.1 to 1.0 mV s^{-1} (Figure 5a), k_1/k_2 analysis was performed to compare the percentage of surface controlled vs. diffusion controlled current responses in NAFO-0.52.[23,24] In k_1/k_2 analysis, the relationship between current i and sweep rate v in surface- ($i \propto v$) and diffusion-controlled ($i \propto v^{1/2}$) mechanisms are qualitatively compared through the proportionality constants k_1 and k_2 as:[23]

$$i(v) = k_1v + k_2v^{1/2}.$$ Eq. S5

Similarly, for reconstructed CVs from SPECS analysis at 0.01 and 0.1 mV s^{-1}, modeled capacitive currents (Figure S11) were taken throughout the voltage window as the capacitive percentage of the total current i_{Total}:

$$\% \text{ surface-controlled } = \frac{i_g + i_p}{i_{Total}},$$ Eq. S6

where i_g is the geometric capacitive current and i_p is the porous capacitive current. The breakdown of contributions of diffusion and capacitive controlled currents are shown in **Figure S12a,** ranging from 81% capacitive-current at 0.01 mV s^{-1} from SPECS analysis to 94% capacitive-current at 1.0 mV s^{-1} from k_1/k_2 analysis. The % capacitive current obtained from SPECS analysis at 0.1 mV s^{-1} corresponds relatively well to that obtained from cyclic voltammetry at the same rate (91 vs 83%, respectively). The corresponding CV at 1.0 mV s^{-1} with the capacitive current region, k_1v, shaded is displayed in **Figure S12b**. SPECS analysis allows for reconstruction of CVs at sweep rates slower than practically obtained though CV. Thus at 0.01 mV s^{-1}, an 81% capacitive current is close to that of an of intrinsic material property without limitations in charge storage that occur when fast sweep rates inflate the capacitive contribution.
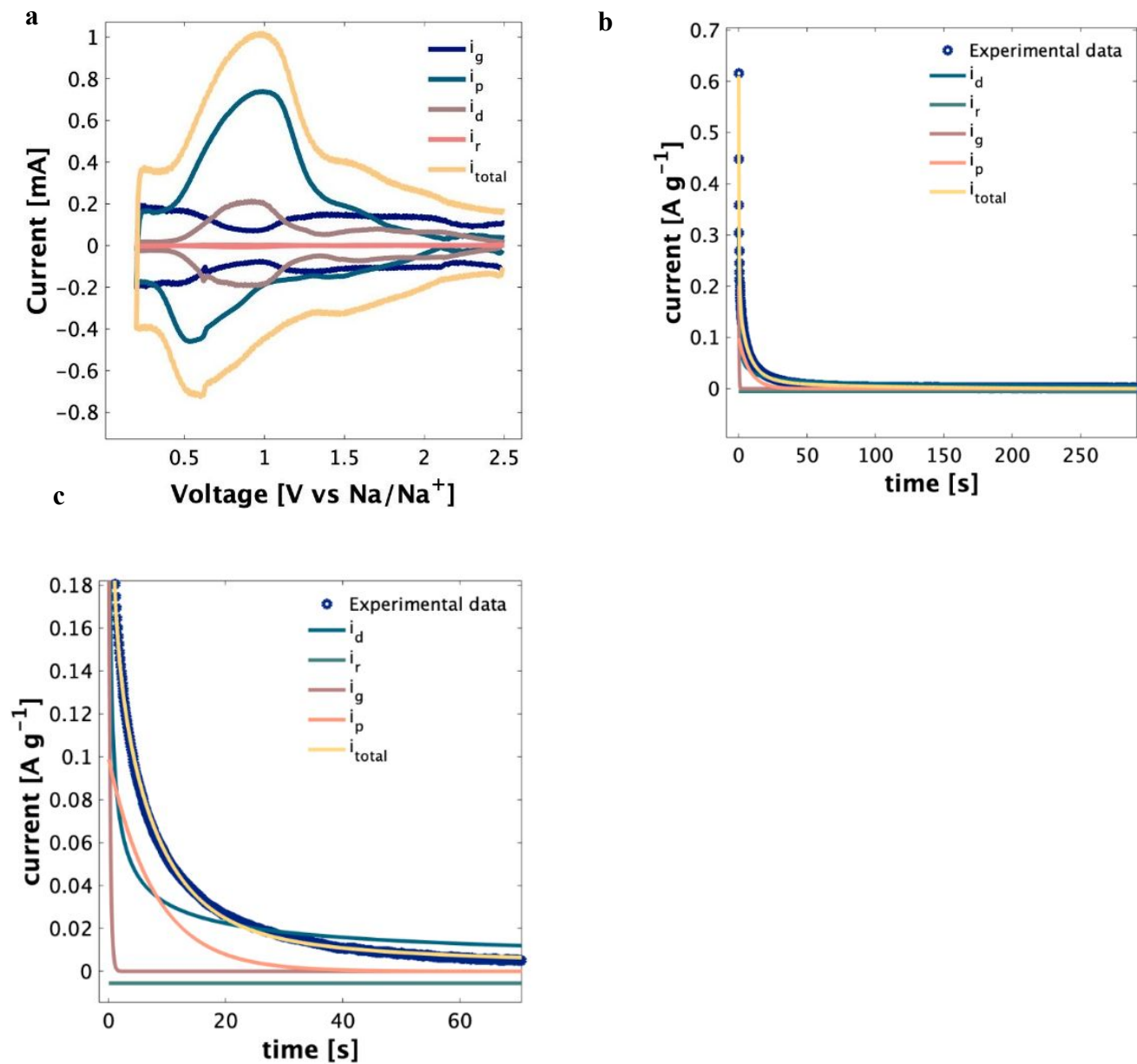
Figure S11 a.) Reconstruction of cyclic voltammetry currents at 0.01 mV s^{-1} based on step-potential electrochemical spectroscopy (SPECS) analysis where i_g is the geometric capacitance current, i_p is the porous capacitance current, i_d is the diffusion controlled current and i_r is the residual current. The high calculated current values of porous capacitance within the redox active voltage region (~0.3-1.2 V vs Na/Na$^+$) confirms the pseudocapacitive nature of the redox process. b) Current decay profile over 300s after a 10 mV voltage step to hold at 0.84 V vs Na/Na$^+$. Currents from SPECS fitting model are shown where i_g is the geometric capacitive current, i_p is the porous capacitive current, i_d is the diffusion-controlled current, i_r is the residual current, and i_{total} is the sum of the modeled currents. c) A

zoomed-in view of the first 50 seconds displaying the short response time for capacitive currents, < 5 s for i_g and < 30 s for i_p, compared to the longer response times for the diffusion controlled current.
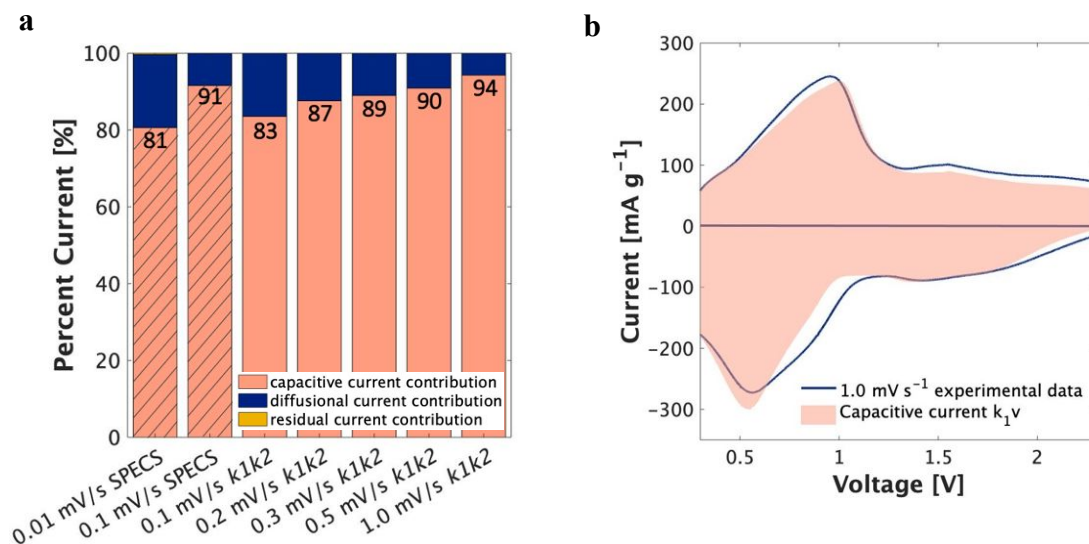

Figure S12. a) Percent capacitive, diffusional, and residual currents of a NAFO-0.52 composite electrode as determined by SPECS and k_1/k_2 analysis. **b)** k_1/k_2 analysis of NAFO-0.52 results in a 94% capacitive current at a scan rate of 1.0 mV s^{-1}.

Table S7. Select data for comparison of normalized capacity in Figure 6.

Material	Approx. C-rate							
	0.5	**1**	**2**	**5**	**10**	**20**	**Loading (mg/cm²)**	**REF**
$Na_3V_2(PO_4)_3$	94	91	80	44	--	--	~1.5	[8]
$Na_3(VO)_2(PO_4)_2F$	130	126	123	108	--	--	~3	[25]
P2 - $Na_{2/3}Mn_{0.8}Fe_{0.1}Ti_{0.1}O_2$	--	93	--	62	46	--	~1	[26]
$NaTi_2(PO_4)_3$	--	68	45	25	--	--	2-3	[11]
$Na_3Fe_2(PO_4)P_2O_7$	51	46	--	40	27	18	~3-4	[10]
NAFO-0.52	67	65	63	59	55	48	1-2	This work

References

(1)   Pearson, W. H.; Lomax, J. F. X-Ray Crystal Diffraction Study of Zr,Na-β-Alumina. *MRS Proc.* **1992**, *293*.

(2)   Bruce, P.; Lisowskaoleksiak, A.; Saidi, M.; Vincent, C. Vacancy Diffusion in the Intercalation Electrode Li1−xNiO2. *Solid State Ion.* **1992**, *57*, 353–358.

(3)   Chen, S.; Wu, C.; Shen, L.; Zhu, C.; Huang, Y.; Xi, K.; Maier, J.; Yu, Y. Challenges and Perspectives for NASICON-Type Electrode Materials for Advanced Sodium-Ion Batteries. *Adv. Mater.* **2017**, *29*, 1700431.

(4)   Zhang, N.; Han, X.; Liu, Y.; Hu, X.; Zhao, Q.; Chen, J. 3D Porous γ-Fe$_2$O$_3$ @C Nanocomposite as High-Performance Anode Material of Na-Ion Batteries. *Adv. Energy Mater.* **2015**, *5*, 1401123.

(5)   Niu, Y.; Xu, M.; Zhang, Y.; Han, J.; Wang, Y.; Li, C. M. Detailed Investigation of a NaTi$_2$(PO$_4$)$_3$ Anode Prepared by Pyro-Synthesis for Na-Ion Batteries. *RSC Adv.* **2016**, *6*, 45605–45611.

(6)   Wang, P.-F.; Yao, H.-R.; Liu, X.-Y.; Yin, Y.-X.; Zhang, J.-N.; Wen, Y.; Yu, X.; Gu, L.; Guo, Y.-G. Na$^+$ /Vacancy Disordering Promises High-Rate Na-Ion Batteries. *Sci. Adv.* **2018**, *4*, eaar6018.

(7)   Lalère, F.; Leriche, J. B.; Courty, M.; Boulineau, S.; Viallet, V.; Masquelier, C.; Seznec, V. An All-Solid State NASICON Sodium Battery Operating at 200 °C. *J. Power Sources* **2014**, *247*, 975–980.

(8)   Böckenfeld, N.; Balducci, A. Determination of Sodium Ion Diffusion Coefficients in Sodium Vanadium Phosphate. *J. Solid State Electrochem.* **2014**, *18*, 959–964.

(9)   Liu, Y.; Zhou, Y.; Zhang, J.; Xia, Y.; Chen, T.; Zhang, S. Monoclinic Phase Na$_3$Fe$_2$(PO$_4$)$_3$: Synthesis, Structure, and Electrochemical Performance as Cathode Material in Sodium-Ion Batteries. *ACS Sustain. Chem. Eng.* **2017**, *5*, 1306–1314.

(10) Cao, Y.; Yang, C.; Liu, Y.; Xia, X.; Zhao, D.; Cao, Y.; Yang, H.; Zhang, J.; Lu, J.; Xia, Y. A New Polyanion Na$_3$Fe$_2$(PO$_4$)P$_2$O$_7$ Cathode with High Electrochemical Performance for Sodium-Ion Batteries. *ACS Energy Lett.* **2020**, *5*, 3788–3796.

(11) Roh, H.-K.; Kim, H.-K.; Kim, M.-S.; Kim, D.-H.; Chung, K. Y.; Roh, K. C.; Kim, K.-B. In Situ Synthesis of Chemically Bonded NaTi2(PO4)3/RGO 2D Nanocomposite for High-Rate Sodium-Ion Batteries. *Nano Res.* **2016**, *9*, 1844–1855. https://doi.org/10.1007/s12274-016-1077-y.

(12) Cava, R. J.; Batlogg, B.; Krajewski, J. J.; Poulsen, H. F.; Gammel, P.; Peck, W. F.; Rupp, L. W. Electrical and Magnetic Properties of Nb 2 O 5 − δ Crystallographic Shear Structures. *Phys. Rev. B* **1991**, *44*, 6973–6981.

(13) Zachauchristiansen, B. Lithium Insertion in Different TiO2 Modifications. *Solid State Ion.* **1988**, *28–30*, 1176–1182. https://doi.org/10.1016/0167-2738(88)90352-9.

(14) Mouahid, F. E.; Bettach, M.; Zahir, M.; Maldonado-Manso, P.; Bruque, S.; Losilla, E. R.; Aranda, M. A. G. Crystal Chemistry and Ion Conductivity of the Na1 + XTi2 − XAlx(PO4)3 (0 ≤ x ≤ 0.9) NASICON Series. *J. Mater. Chem.* **2000**, *10*, 2748–2757.

(15) Goodenough, J. B.; Hong, H. Y.-P.; Kafalas, J. A. Fast Na+-Ion Transport in Skeleton Structures. *Mater. Res. Bull.* **1976**, *11*, 203–220.

(16) Song, S.; Duong, H. M.; Korsunsky, A. M.; Hu, N.; Lu, L. A Na+ Superionic Conductor for Room-Temperature Sodium Batteries. *Sci. Rep.* **2016**, *6* (1), 32330.

(17) Boukamp, B. A.; Huggins, R. A. Fast Ionic Conductivity in Lithium Nitride. *Mater. Res. Bull.* **1978**, *13*, 23–32.

(18) Properties of Ionotec beta"-auminas http://www.ionotec.com/pdfs/NaKbetaceramics.pdf.

(19) Forghani, M.; Mavroudis, H.; McCarthy, J.; Donne, S. W. Electroanalytical Characterization of Electrochemical Capacitor Systems Using Step Potential Electrochemical Spectroscopy. *Electrochimica Acta* **2020**, *332*, 135508.

(20) Dupont, M. F.; Donne, S. W. Charge Storage Mechanisms in Electrochemical Capacitors: Effects of Electrode Properties on Performance. *J. Power Sources* **2016**, *326*, 613–623.

(21) Dupont, M. F.; Donne, S. W. Electrolytic Manganese Dioxide Structural and Morphological Effects on Capacitive Performance. *Electrochimica Acta* **2016**, *191*, 479–490.

(22) Forghani, M.; Donne, S. W. Modification of the Step Potential Electrochemical Spectroscopy Analysis Protocol to Improve Outcomes. *J. Electrochem. Soc.* **2019**, *166*, A2727–A2735.

(23) Choi, C.; Ashby, D. S.; Butts, D. M.; DeBlock, R. H.; Wei, Q.; Lau, J.; Dunn, B. Achieving High Energy Density and High Power Density with Pseudocapacitive Materials. *Nat. Rev. Mater.* **2020**, *5*, 5–19.

(24) Liu, T.-C. Behavior of Molybdenum Nitrides as Materials for Electrochemical Capacitors. *J. Electrochem. Soc.* **1998**, *145*, 1882.

(25) Chao, D.; Lai, C.-H. M.; Liang, P.; Wei, Q.; Wang, Y.-S.; Zhu, C. R.; Deng, G.; Doan-Nguyen, V. V. T.; Lin, J.; Mai, L.; Fan, H. J.; Dunn, B.; Shen, Z. X. Sodium Vanadium Fluorophosphates (NVOPF) Array Cathode Designed for High-Rate Full Sodium Ion Storage Device. *Adv. Energy Mater.* **2018**, *8*, 1800058.

(26) Han, M. H.; Gonzalo, E.; Sharma, N.; López del Amo, J. M.; Armand, M.; Avdeev, M.; Saiz Garitaonandia, J. J.; Rojo, T. High-Performance P2-Phase $Na_{2/3}Mn_{0.8}Fe_{0.1}Ti_{0.1}O_2$ Cathode Material for Ambient-Temperature Sodium-Ion Batteries. *Chem. Mater.* **2016**, *28*, 106–116.